This is a non-peer-reviewed preprint submitted to EarthArXiv. The original manuscript has been submitted to GSA Bulletin and has not yet undergone peer review by the Geological Society of America

---

Constraining the paleoclimate and paleoecology of the Selandian – Thanetian transition in the Lower Wilcox, Texas Gulf Coast

Nikhil Sharma[1, 2*], Vann Smith[3], Lorena G. Moscardelli[1], Thierry Adatte[4], Lucas Vimpere[5], Iulia Olariu[1], William A. Ambrose[1], David Bord[6], Victor Giraldo-Gómez[3], Maria A. Lorente[3], Brahimsamba Bomou[4], Laszlo Kocsis[7]

[1]Bureau of Economic Geology, Jackson School of Geosciences, The University of Texas at Austin, P.O. Box X, Austin, Texas 78713-8924, USA

[2]Department of Geosciences, Swedish Museum of Natural History, Box 50007, SE-104 05 Stockholm, Sweden

[3]Ellington Geological Services, 1414 Lumpkin Road, Houston, Texas 77043, USA

[4]Institute of Earth Sciences (ISTE), University of Lausanne, Lausanne 1015, Switzerland

[5]Department of Earth Sciences, University of Geneva, 1205 Geneva, Switzerland

[6]BP America, Inc., 200 Westlake Park Blvd, Houston, Texas 77079, USA

[7]Institute of Earth Surface Dynamics (IDYST), University of Lausanne, Lausanne 1015, Switzerland

ABSTRACT

The Selandian–Thanetian Transition Event (STTE) represents a relatively understudied interval of carbon cycle instability and environmental disruption during the Paleocene. This study presents a comprehensive sedimentological, palynological, and geochemical record of the STTE based on two shallow marine wells (Moczygemba VT #11 and Vogelsang Frieda #1) from the Texas Gulf Coast. Our multi-proxy approach integrates palynology and nannofossil biostratigraphy to establish age constraints and track ecological changes, organic carbon isotopes to detect regional preservation of the STTE, and use elemental ratios to infer chemical weathering intensity and mean annual precipitation. Results indicate that the STTE along the Gulf Coast was characterized by elevated weathering rates under semi-arid to humid climatic conditions. Palynological assemblages show a marked increase in *Thomsonipollis magnificus*, suggesting the expansion of mangrove or coastal swamp taxa during inferred warming phases. Notably, negative excursions in organic carbon isotopes, along with increased terrestrial input of organic matter in both cores, confirm the regional expression and impact of the STTE. These findings provide critical constraints on the Selandian–Thanetian Transition Event by linking carbon cycle perturbations to continental-scale source-to-sink responses across North America, and demonstrate how deltaic systems along the Gulf Coast recorded and responded to mid-Paleocene global warming.

INTRODUCTION

The Paleocene Epoch (66–56 Ma) was characterized by repeated, short-lived perturbations in the global carbon cycle, culminating in the well-documented Paleocene–Eocene Thermal Maximum (PETM; Zachos et al., 2008). Prior to the PETM, other transient warming events have been recognized in both marine and terrestrial records. One such event is the early late Paleocene hyperthermal (ELPE; Bralower et al., 2002), also referred to as the mid-Paleocene biotic event (MPBE; Bernaola et al., 2007). This climatic perturbation occurred near the boundary of the Selandian and Thanetian stages and has been identified in multiple deep-sea cores including Shatsky Rise (ODP Leg 198), Walvis Ridge (ODP Leg 208), Maud Rise (ODP Leg 113), and Black Nose (ODP Leg 171) as well as in several onshore and terrestrial sections across Europe, North Africa, and the Southern Hemisphere (e.g., Zumaia, Contessa Road, Tejerouine, Ouled Abdoun, Naqb El-Rufuf, Mead Stream, Cerro Bayo) (Bralower et al., 2002; Zachos et al., 2004; Petrizzo, 2005; Bernaola et al., 2007; Westerhold et al., 2011; Coccioni et al., 2012; Karoui-Yaakoub et al., 2014; Kocsis et al., 2014; Littler et al., 2014; Pujalte et al., 2014, 2016; Hyland et al., 2015; Hewaidy et al., 2019).

In the Tethyan realm, biotic and environmental changes across this interval have been collectively termed the Selandian–Thanetian Transition Event (STTE) by Coccioni et al. (2012). However, the precise stratigraphic and causal relationships among the STTE, ELPE, and MPBE remain poorly understood (Coccioni et al., 2019).

The STTE is marked by negative carbon isotope excursions (CIEs), biotic turnover, and oceanographic reorganization, suggesting transient climate warming and disruption of the global carbon cycle (Bornemann et al., 2009). Proposed mechanisms include volcanic outgassing, methane hydrate destabilization, and oxidation of organic carbon (Sluijs et al., 2007). While the magnitude of the STTE was smaller than that of the PETM, which involved >5°C global warming and major ecosystem restructuring (McInerney & Wing, 2011), it perhaps reflects preconditioning processes in the Earth system (Maufrangeas et al., 2020).

Recent studies using high-resolution carbon isotope stratigraphy have documented multiphase carbon cycle perturbations during the late Selandian–early Thanetian, pointing to complex interactions between carbon sources and sinks (Westerhold et al., 2011; Maufrangeas et al., 2020). Paleoceanographic proxies suggest parallel changes in ocean circulation, oxygenation, and productivity that may have modulated the climatic response (Bornemann et al., 2009).

Both marine and terrestrial records now provide growing evidence for the global extent of the STTE. In marine settings, changes in nannofossil and foraminiferal assemblages along with shifts in carbonate content and magnetic susceptibility are observed at sites such as Contessa Road (Italy) and Naqb El-Rufuf (Egypt) (Coccioni et al., 2019; Hewaidy et al., 2019). On land, paleosol carbon isotope excursions and changes in vegetation indicate transient warming and hydrological shifts. At Cerro Bayo (Argentina), the STTE is preserved as a two-stage hyperthermal event (Hyland et al., 2015), while the Lairière section in the Pyrenees reveals CIEs within fluvio-lacustrine strata correlated to global events (Maufrangeas et al., 2020).

In this study, we evaluate whether the Selandian–Thanetian Transition Event is recorded in a shallow marine delta system along the Texas Gulf Coast. We test the hypothesis that carbon cycle instability is reflected in negative $\delta^{13}C$ excursions, alongside shifts in vegetation, weathering intensity, and precipitation. Using a multi-proxy approach that integrates palynological, calcareous nannofossil, and geochemical data, we examine two shallow marine wells (Moczygemba VT #11 and Vogelsang Frieda #1). Although coastal-deltaic environments are susceptible to sedimentary discontinuities, our results reveal a coherent STTE signal. Given the Gulf Coast's role in North American sediment routing, this study offers insights into source-to-sink dynamics and how marginal marine systems recorded mid-Paleocene climate perturbations at a continental scale.

GEOLOGICAL SETTING, STRATIGRAPHY AND AGE CONSTRAINTS

Sediment routing along the Texas Gulf Coast

During the Selandian-Thanetian, large-scale fluvial systems primarily controlled sediment routing along the Texas Gulf Coast, transporting siliciclastic sediments from the North American continental interior to the Gulf of Mexico (Galloway et al., 2000; Galloway et al., 2011; Hessler et al., 2017). The Laramide Orogeny in NW-USA during the Paleogene played a key role in reshaping North American drainage patterns, generating significant hinterland relief and initiating continental-scale sediment transport (Blum and Pecha, 2014; Sharman et al., 2017). A limited number of major fluvial axes delivered these sediments, each forming large prograding deltaic depocenters in the Gulf Basin (Galloway et al., 2011).

The paleo-Colorado rivers were dominant transport systems, with the Colorado axis serving as a primary Laramide-era drainage route during Wilcox time. The paleo-Colorado River, with an estimated 2×10^6 km^2 catchment area and sediment load of ca. 290 Mt/yr, supplied material to deltaic depocenters in the Rockdale delta system within the Houston embayment (Fisher and McGowen, 1967; Sweet and Blum, 2012). Detrital zircon U-Pb data confirm sediment sources from the Southern Rockies, Cordilleran arc, and northern Mexico (Galloway et al., 2011).

The Texas Wilcox Group represents the first major influx of Laramide-derived siliciclastic sediments into the Gulf Basin, marking a shift in sedimentation as fluvial systems expanded southward and bypassed overfilled Laramide basins (Galloway et al., 2011). This influx was significant, with sediment flux exceeding 150,000 km^3/Ma, one of the highest multi-million-year depositional episodes recorded for the Gulf of Mexico (Galloway et al., 2000). The Wilcox Group is subdivided into the Lower, Middle, and Upper Wilcox depositional episodes, with the Middle

Wilcox being overlain by the broad marine Yoakum Shale, commonly associated with the Paleocene-Eocene boundary (Galloway, 2008; Vimpere et al., 2023).

The Rockdale delta system acted as a major depocenter, with multiple distributary channels transporting material across a broad shelf setting under greenhouse conditions (see figure 1 of Zeng and Olariu, 2024). Sediment supply fluctuations, eustatic sea-level changes, and subsidence rates influenced transgressive–regressive (T-R) cycles, generating complex stratigraphic stacking patterns (Zhang et al., 2018). Paleoclimatic shifts also played a key role in modulating sediment supply, with geochemical proxies indicating variations in hinterland weathering intensity. Warmer intervals were associated with intensified chemical weathering and increased clay input, while fluctuations in riverine discharge affected delta progradation and shoreline migration (Hessler et al., 2017; Vimpere et al., 2023).

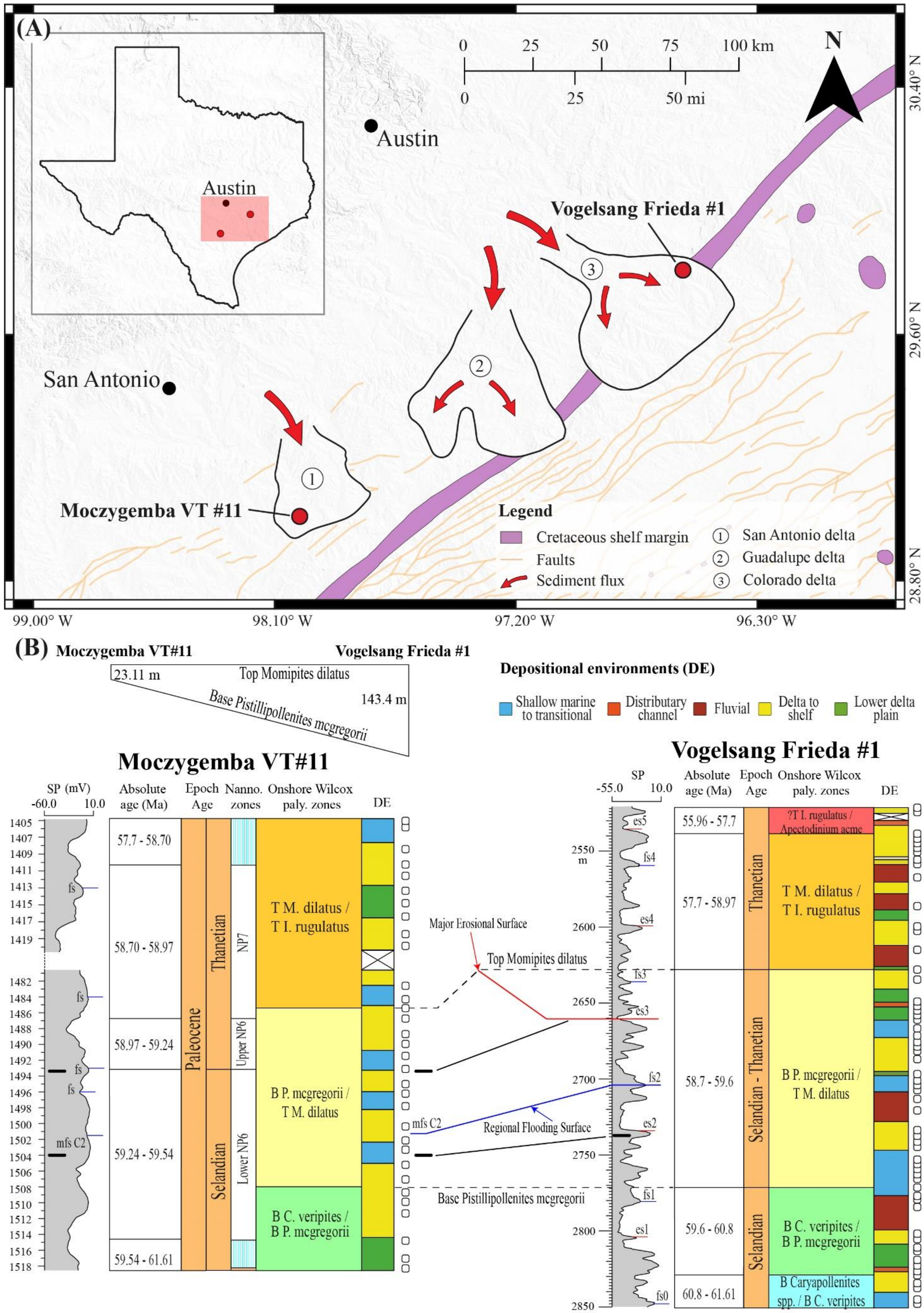
(A)
Austin
San Antonio
Vogelsang Frieda #1
Moczygemba VT #11
0 25 50 75 100 km
0 25 50 mi
N
30.40° N
29.60° N
28.80° N
99.00° W
98.10° W
97.20° W
96.30° W
Legend
Cretaceous shelf margin
Faults
Sediment flux
① San Antonio delta
② Guadalupe delta
③ Colorado delta
(B) Moczygemba VT#11
Vogelsang Frieda #1
23.11 m
Top Momipites dilatus
Base Pistillipollenites mcgregorii
143.4 m
Depositional environments (DE)
Shallow marine to transitional
Distributary channel
Fluvial
Delta to shelf
Lower delta plain
Moczygemba VT#11
SP (mV)
Absolute age (Ma)
Epoch Age
Nanno. zones
Onshore Wilcox paly. zones
DE
57.7 - 58.70
58.70 - 58.97
58.97 - 59.24
59.24 - 59.54
59.54 - 61.61
Paleocene
Thanetian
Selandian
NP7
Upper NP6
Lower NP6
T M. dilatus / T I. rugulatus
B P. mcgregorii / T M. dilatus
B C. veripites / B P. mcgregorii
mfs C2
Major Erosional Surface
Top Momipites dilatus
Regional Flooding Surface
Base Pistillipollenites mcgregorii
Vogelsang Frieda #1
55.96 - 57.7
57.7 - 58.97
58.7 - 59.6
59.6 - 60.8
60.8 - 61.61
Thanetian
Selandian - Thanetian
Selandian
?T I. rugulatus / Apectodinium acme
T M. dilatus / T I. rugulatus
B P. mcgregorii / T M. dilatus
B C. veripites / B P. mcgregorii
B Caryapollenites spp. / B C. veripites

Figure 1. Map, depositional framework and stratigraphy of the study area. (A) Regional map of Texas highlighting the Moczygemba VT#11 (San Antonio Delta) and Vogelsang Freida #1 (Colorado Delta) wells. Major sediment flux pathways (red arrows), the Cretaceous shelf margin (purple line), and major growth fault zones (orange lines) are shown. Growth faults dip southeast. (B) Stratigraphic sections with self-potential logs, absolute ages, biozones (nannofossil and palynological), and interpreted depositional environments (shallow marine, transitional, deltaic distributary and fluvial channels, delta-shelf transition, and lower delta plain). SP log trends (coarsening- or fining-upward) help define transgressive and regressive intervals, marked by flooding surfaces (FS), maximum flooding surfaces (MFS), and erosional surfaces (ES). Dotted lines indicate biostratigraphic boundaries; black solid lines mark key surface correlations (FS, ES); blue line = MFS C2; red line = major erosional surface (ES3) at the base of the Colorado Delta. White circles mark sample locations. Vertical scales differ between wells.

Stratigraphic arrangement

The Moczygemba VT #11 and Vogelsang Frieda #1 cores provide valuable records of the Lower Wilcox Rockdale Delta system, which consists of eight depocenters reaching thicknesses of up to 1500 m (Fisher and McGowen, 1967; Zeng and Olariu, 2024). The Vogelsang Frieda #1 core sampled the Colorado Delta, while the Moczygemba #11 core is within the San Antonio Delta (Fig. 1). The biostratigraphic correlation is defined by time lines represented in Figure 1 by the base of *Pistillipollenites mcgregorii* and the top of *Momipites dilatus*. The biostratigraphic correlation clearly indicates that there is an expanded stratigraphic section toward the north east associated with the Colorado Delta implying higher sedimentation rates in this region.

The Vogelsang Frieda #1 core, spanning 685 m, records 14 transgressive–regressive cycles, with individual cycle thickness ranging from 18 to 110 m (Zhang et al., 2022). These cycles document alternating phases of delta progradation and marine transgression, driven by changes in sediment supply, relative sea level, and coastal dynamics. Wave-dominated deposits constitute the largest proportion (48%) of the Vogelsang core stratigraphy, followed by river-dominated deposits (40%) and tide-influenced facies (12%). Each T-R cycle progresses from wave- or river-dominated delta-front deposits (9–75 m thick) to fluvial or fluvial-tidal channel fills (8–33 m thick), capped by wave- or tide-dominated transgressive deposits (3–30 m thick) (Zhang et al., 2022) (Fig. 1). Lithologically, both cores consist of interbedded sandstones, siltstones, and mudstones with organic-rich horizons and bioturbated intervals. Sandstone intervals feature sedimentary structures such as hummocky cross-stratification (HCS), swaley cross-stratification (SCS), and wave ripples, indicating storm-wave reworking of deltaic and shoreface sands. Thin tidal rhythmites within heterolithic deposits suggest intermittent tidal influence in estuarine settings (Galloway et al., 2000; Zhang et al., 2022).

The supplementary material accompanying this manuscript provides further details on the depositional environments of Moczygemba VT #11 and Vogelsang Frieda #1 cores.

Age model

Age control for both wells is provided by nannofossil biostratigraphy (Moczygemba VT #11 only) and palynological biostratigraphy (both Moczygemba VT #11 and Vogelsang Frieda #1). Estimated absolute ages are based on Geologic Time Scale 2012 (Gradstein et al. 2012) ages for nannofossil events and based on Crabaugh and Elsik (2000), Elsik and Crabaugh (2001), and Zarra et al. (2019) for palynological events. The calcareous nannofossil biozonation follows Martini

(1971) and the palynological biozonation follows Zarra et al. (2019). Absolute ages for T *Insulapollenites rugulatus* and B *Pistillipollenites mcgregorii* in Zarra et al. (2019) were estimated based on their height relative to the chronostratigraphic column. An age model based on the biostratigraphic data is provided in the Supplementary Materials. We provide absolute age estimates as minimum and maximum ages for each sample; ages with higher uncertainties appear in parentheses.

MATERIAL AND METHODS

Sample collection

Core samples were collected for palynological and geochemical analysis from both the Moczygemba VT #11 and Vogelsang Frieda #1 wells (Fig. 1, Supplementary Material).

Palynology

All palynological samples were subjected to standard acid preparation involving treatment with warm hydrochloric acid (HCl) to remove carbonates and warm hydrofluoric acid (HF) to dissolve silicates. Processing techniques are similar to those described by Traverse (2007). If sufficient organic matter was present, three slides were produced per sample, the first containing an un-sieved and unoxidized fraction for kerogen analysis, and the other two oxidized and sieved with a 10 µm aperture nylon mesh for palynological analysis. For lower abundance samples (<300 palynomorphs in a slide), all specimens were counted; for higher abundance samples, a modified version of the cascading count technique described by Styzen (1997) was used to estimate the total number of palynomorph specimens present on the slide.

For Moczygemba VT #11, the full palynological counts were simplified for linear discriminant analysis (LDA) using the PAleontological STatistics (PAST) software (Hammer et al. 2001). Vogelsang Frieda #1 was not analyzed using LDA because of generally lower palynomorph abundances which introduce more statistical noise. Due to low dinoflagellate cyst abundances in Moczygemba VT #11, all dinoflagellate cyst taxa have been combined into a single type ("total dinoflagellate cysts"). Fungal hyphae have been excluded from the analysis and all other fungal remains have likewise been combined into a single type ("fungal remains"). Algal remains aside from dinoflagellate cysts and acritarchs have been excluded from the analysis. Pollen and plant spore taxa with less than 200 total occurrences in Moczygemba VT #11 have been excluded from analysis. These rare taxa were excluded to ensure that there were a higher number of samples than variables (i.e., taxa) in the matrix, and because abundance counts of rare taxa are inherently more prone to random variability. The simplified palynological counts for both wells and detailed results for the linear discriminant analysis are provided in the Supplementary Materials.

Micropaleontology

A total of 28 samples from the Vogelsang Frieda #1 core were analyzed for foraminifera. The original samples and disaggregated residues were weighted, and all samples were washed in water over a 63 μm sieve and dried in an oven. All specimens were selected, systematically counted, and mounted on a microslide. The absolute abundance of foraminifera was obtained by standardizing to 1 gram of sediment (forams/1 gr Sed).

Rock-Eval pyrolysis

The quality and quantity of organic matter (OM) was analyzed in 97 bulk sample powders using a Rock-Eval 6 instrument at the Institute of Earth Sciences, University of Lausanne (ISTE-UNIL), following the methodology outlined by Behar et al. (2001) and utilizing the IFP 160 000 standard. Sample aliquots were placed in an oven and initially heated to 300°C under an inert atmosphere before undergoing gradual pyrolysis up to 650°C. After pyrolysis, the samples were transferred to another oven and progressively heated to 850°C in the presence of air, with CO_2 and hydrocarbon (HC) concentrations monitored throughout the process. The calculated parameters included total organic carbon content (TOC, wt.%), hydrogen index (HI in mg HC g^{-1} TOC), oxygen index (OI in mg CO_2 g^{-1} TOC), and T_{max} (°C), following the methods of Espitalié et al. (1985) and Behar et al. (2001).

Organic carbon isotopes

The carbon isotope composition of organic matter ($\delta^{13}C_{org}$) in 155 samples was determined at the stable isotope laboratory of the Institute of Earth Surface Dynamics, University of Lausanne (IDYST-UNIL). Samples were first decarbonated using 10% v/v HCl, then thoroughly washed with deionized water and dried at 40°C for 48 hours. $\delta^{13}C_{org}$ measurements were conducted using a Carlo Erba 1100 (Fisons Instruments, Milan, Italy) elemental analyzer, coupled to a Thermo Fisher Scientific Delta V Plus isotope ratio mass spectrometer, both operating under continuous helium flow. The measured $\delta^{13}C$ values were calibrated and normalized using international reference materials and in-house standards (Spangenberg, 2006, 2016) and are reported in per mil (‰) relative to the Vienna Pee Dee Belemnite limestone standard (VPDB). The precision of $\delta^{13}C_{org}$ values was better than 0.1‰.

X-ray Fluorescence (XRF) analysis

Major element concentrations were determined using a Bruker Tracer IV ED-XRF instrument equipped with an Rh x-ray tube and pXRF technology and excitation voltage of 15 kV, at the Bureau of Economic Geology, UT Austin, Texas. The instrument operated with a He purge and utilized a filter composed of 0.006-inch Cu and 0.001-inch Ti. Before analysis, the core was cleaned with hot water and a plastic brush to eliminate potential contaminants like salts that might have crystallized over time. The pXRF scans were regularly checked for Cl peaks, which could interfere with the Compton peak used in peak normalizations. Samples showing excessive Cl were cleaned again and reanalyzed. Calibration of the pXRF measurements was conducted using semiquantitative methods described by Rowe et al. (2012).

Paleo-weathering

To evaluate weathering trends, we applied established weathering proxies that have been used on both terrestrial and marine sediments (e.g., Hessler et al., 2017; Deng et al., 2022; Sharma et al., 2024), including the Chemical Index of Alteration (CIA, in %, Eq. 1) and the Chemical Index of Weathering (CIW, in %, Eq. 2), originally proposed by Nesbitt and Young (1982) and Harnois (1988), respectively.

The CIA was used to quantify the degree of weathering by calculating the molar ratio of immobile Al_2O_3 to the mobile oxides CaO, Na_2O, and K_2O within the silicate fraction. The CIA is also used to evaluate environmental factors such as temperature, precipitation, elevation, and slope, which influence silicate weathering.

$$\mathrm{CIA} = \frac{\mathrm{Al_2O_3}}{\mathrm{Al_2O_3} + +\mathrm{Na_2O} + \mathrm{CaO^*} + \mathrm{K_2O}} \times 100 \quad (1)$$

Where CaO^* represents the CaO incorporated in the silicate fraction and is determined as: $CaO^* = CaO - (10/3 \times P_2O_5)$.

Under intense weathering, mobile oxides are removed, leading to an increased concentration of Al_2O_3, with CIA values approaching nearly 100 wt.%. Conversely, weak weathering results in lower CIA values (<50%) due to the prevalence of mobile oxides.

For comparison, we also applied the CIW, which is a modified version of the CIA, designed to account for potassium metasomatism in sediments (e.g., Stein et al., 2021).

$$\mathrm{CIW} = \frac{\mathrm{Al_2O_3}}{\mathrm{Al_2O_3} \; + \; +\mathrm{Na_2O} + \mathrm{CaO^*}} \times 100 \qquad (2)$$

Mean annual precipitation

Mean annual precipitation (MAP, in mm yr^{-1}, Eq. 3) was estimated using the CIW (Eq. 2) and is based on the equation proposed by Sheldon et al. (2002), with a standard error of ±182 mm yr^{-1}.

$$\mathrm{MAP} = 221e^{0.0197(\mathrm{CIW})} \qquad (3)$$

Uncertainty estimates

All data presented in this study include uncertainties expressed as the standard error of the mean (SE), calculated using the formula SE = SD/√n, where SD represents the standard deviation and *n* is the number of replicates analyzed. Although uncertainty estimates are provided, they are often not clearly visible on the plots due to their small magnitude relative to the plot scale.

RESULTS

Biostratigraphy

Palynological biostratigraphy is largely based on the biostratigraphic scheme developed by Zarra et al. (2019) for the deepwater Wilcox. However, it was found that an event-based biostratigraphy was more suitable to the studied onshore Lower Wilcox (Smith et al., 2025; in press) wells than the largely assemblage-based zonation in Zarra et al. (2019). An alternative palynological zonation for the onshore Lower Wilcox, with the boundaries defined by individual events, has therefore been used.

Aside from the events "T *Momipites dilatus*" and "T *Caryapollenites* spp.," the other zonal boundaries in our alternative zonation are used as markers in Zarra et al. (2019). "T *Momipites dilatus*" and "B *Caryapollenites* spp." (considered synonymous with "*Carya* spp. <30 µm Base") were used by Crabaugh and Elsik (2000) and Elsik and Crabaugh (2001) in their onshore Wilcox Group zonation. "T *Momipites dilatus*" is early Thanetian in age, near the top of the lower Wilcox as defined by Crabaugh and Elsik (2000). "T *Caryapollenites* spp." is earliest Selandian in age, slightly above the Midway Group/Wilcox Group boundary. For the purposes of this study, we have only used previously published biostratigraphic events.

The top analyzed sample in Moczygemba VT #11 at 1405.13 mbs (meters below surface) is Thanetian in age, in the "T *Momipites dilatus*/T *Insulapollenites rugulatus*" zone (Fig. 1). Nannofossil recovery in the top three analyzed samples in Moczygemba VT #11 was insufficient for age determination. The highest sample with sufficient nannofossil recovery is at 1410.74 mbs and is in nannofossil zone NP7. "T *Momipites dilatus*" was observed at 1485.60 mbs, slightly above the NP6/NP7 boundary at 1486.81 mbs. The lower NP6/upper NP6 boundary at 1492.81 mbs is an approximate marker for the Selandian/Thanetian boundary. The primary palynological marker event "B *Pistillipollenites mcgregorii*" was observed at 1508.61 mbs, slightly above the questionable base of NP6 at 1513.23 mbs (Fig. 1). The sample at 1516.79 mbs contains a probably

NP5 age nannofossil assemblage and the observed base of multiple palynomorph species, including the primary marker event "B *Caryapollenites veripites*." A large (ca.300 m) sample gap between 1516.79 mbs and 1843.13 has been left unzoned. However, this large unsampled section is constrained to be Selandian in age based on the presence of *Caryapollenites* spp. in downsection samples. Nannofossil recovery in the bottom section below the large sample gap is insufficient for age determination, but based on the presence of *Caryapollenites imparalis* in the bottom sample (1851 mbs), the bottom section is early Selandian in age, in the "B *Caryapollenites* spp./B *Caryapollenites veripites*" zone.

Vogelsang Frieda #1 was not sampled for nannofossil analysis and biostratigraphic age control relies on palynology. Although the recovery and preservation of palynomorphs was generally better in the Moczygemba VT #11 samples, the relatively high and continuous sampling resolution in Vogelsang Frieda #1 makes it an excellent reference well for palynological biostratigraphy. Near the top of the analyzed section at 8328.50 mbs, the primary marker "T *Insulapollenites rugulatus*" was observed, possibly below its true stratigraphic top. The top two samples (at 8272 mbs and 8282 mbs) are questionably in the Thanetian "T *Insulapollenites rugulatus*/*Apectodinium* acme" zone, the uncertainty resulting from the rarity of the marker taxon *I. rugulatus* near its top and the fairly low abundances in the top two samples. "T *Momipites dilatus*," an early Thanetian marker, was observed at 8622 mbs. Palynological biostratigraphy is not able to precisely delineate the Selandian/Thanetian boundary, but it lies within the "B *Pistillipollenites mcgregorii*/T *Momipites dilatus* zone (8622-9092.50 mbs) (Fig. 1). The primary marker "B *Caryapollenites veripites*" was observed at 9275 mbs, at the same depth as the base of *Spinaepollis spinosa* and *Momipites triradiatus* type, possibly suggestive of an unconformity between 9275.00 – 9281.50 mbs. Below 9275 mbs, palynological abundances are generally lower than upsection, reducing the confidence in the placement of bioevents below 9275 mbs. The earliest Selandian event "B *Caryapollenites* spp." was questionably observed near the base of the analyzed section at 10488 mbs; only a single downsection sample was analyzed, and the absence of *Caryapollenites* spp. in that sample may be due to low general palynomorph abundance rather than true regional absence.

Foraminiferal assemblages

The foraminiferal assemblages studied in the Vogelsang Frieda #1 core determined that in all the samples analyzed only benthic foraminifera were found, of which practically all are agglutinated foraminifera such as *Haplophragmoides* spp., *Reophax* sp, and *Ammobaculites* sp. Most of the analyzed foraminifera display poor preservation characterized by pyritized tests, in which sutures and chambers are not recognizable.

Organic matter content and characterization

The total organic carbon (TOC) content in both sections has an average value of 1.75 ± 0.09 wt.% (N = 155). In the Moczygemba section, TOC values range from 0.24 ± 0.09 to 4.95 ± 0.09 wt.%, averaging 1.78 ± 0.09 wt.% (N = 109). In contrast, TOC values in the Vogelsang section range from 0.67 ± 0.22 to 6.76 ± 0.22 wt.%, with an average of 1.83 ± 0.22 wt.% (N = 46).

To classify organic matter (OM) by type (origin) and thermal maturity, T_{max} values and hydrogen index (HI)/oxygen index (OI) ratios were analyzed (Espitalié et al., 1985). T_{max} values range from 418 to 446°C, suggesting that the preserved OM is predominantly immature or within the oil window (Fig. 2). HI values in both Moczygemba and Vogelsang are generally below 200 mg HC/g TOC (average 96.25 mg HC/g TOC), indicating that the OM is primarily Type III and IV, characteristic of a strong terrestrial plant input.

OI values are lower compared to HI, generally remaining below 100 mg CO_2/g TOC (average 42.5 mg CO_2/g TOC), expect two samples which have values up to 150 mg CO_2/g TOC. Overall, the Rock-Eval parameters suggest that the organic matter in both sections (Moczygemba and Vogelsang) originates from a recycled and/or terrestrial source.

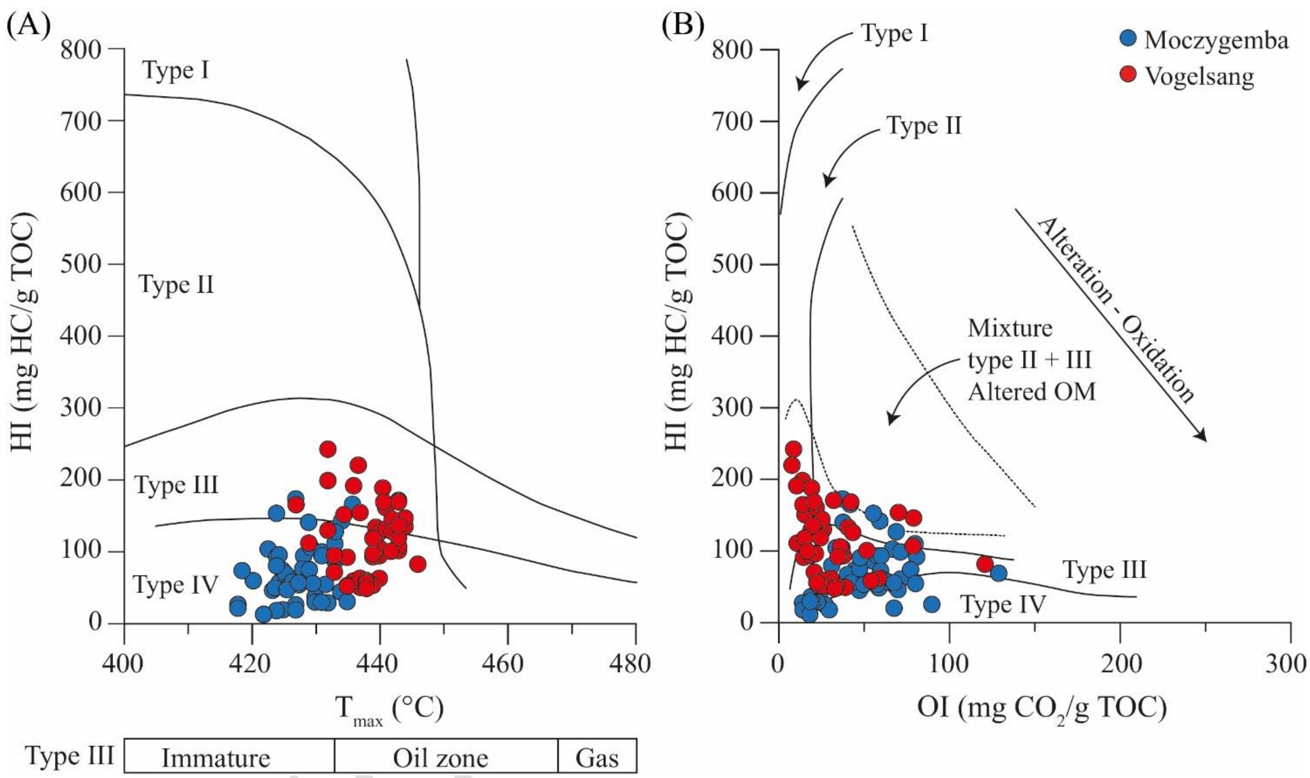

Figure 2. Kerogen type and thermal maturity assessment of organic matter. (A) Hydrogen Index (HI) vs. T_{max} plot showing the classification of kerogen types (I–IV) and thermal maturity for Moczygemba (blue circles) and Vogelsang (red circles) samples. Most samples classify as Type III or Type IV (immature and oil zone) organic matter. (B) Hydrogen Index (HI) vs. Oxygen Index (OI) plot illustrating the kerogen type distribution and the effects of oxidation and alteration. The majority of samples cluster in the Type III–IV range.

Organic carbon isotopes

The organic carbon isotope ($\delta^{13}C_{org}$) records from the Moczygemba VT #11 and Vogelsang Frieda #1 cores provide insights into the carbon cycle dynamics across the Selandian-Thanetian transition. These data offer valuable constraints on paleoenvironmental conditions and potential climatic perturbations during the Paleocene.

The $\delta^{13}C_{org}$ records from the two cores exhibit distinct yet comparable trends across the studied stratigraphic intervals. In Moczygemba VT #11, values range between -27.0 ± 0.02 and -25.5 ± 0.02‰ VPDB (average value of -26.2 ± 0.02‰; N = 109), displaying notable fluctuations. A pronounced negative carbon isotope excursion (CIE) of 0.5‰ magnitude is identified between depths 1498–1504 m, followed by a subsequent recovery until 1494 m and a second negative CIE of 0.4‰ magnitude between depths 1486 – 1494 m. These negative shifts suggest a perturbation in the global carbon cycle, or may reflect changes in carbon sources or burial processes (Fig. 3).

In Vogelsang Frieda #1, $\delta^{13}C_{org}$ values range between -28.0 ± 0.06 and -25.5 ± 0.06‰ VPDB (average value of -26.6 ± 0.06‰; N = 46), with slightly more negative values compared to Moczygemba VT #11. A negative CIE of ca.1‰ magnitude is evident in the lower part of the section (2700–2750 m) spanning the Selandian-Thanetian transition, closely corresponding to the negative excursion observed in Moczygemba VT #11. A major erosional surface in Vogelsang Frieda #1 coincides with another possible negative shift of 0.2‰ magnitude, noted between depths 2650–2670 m, though its exact stratigraphic correlation remains uncertain (Fig. 3).

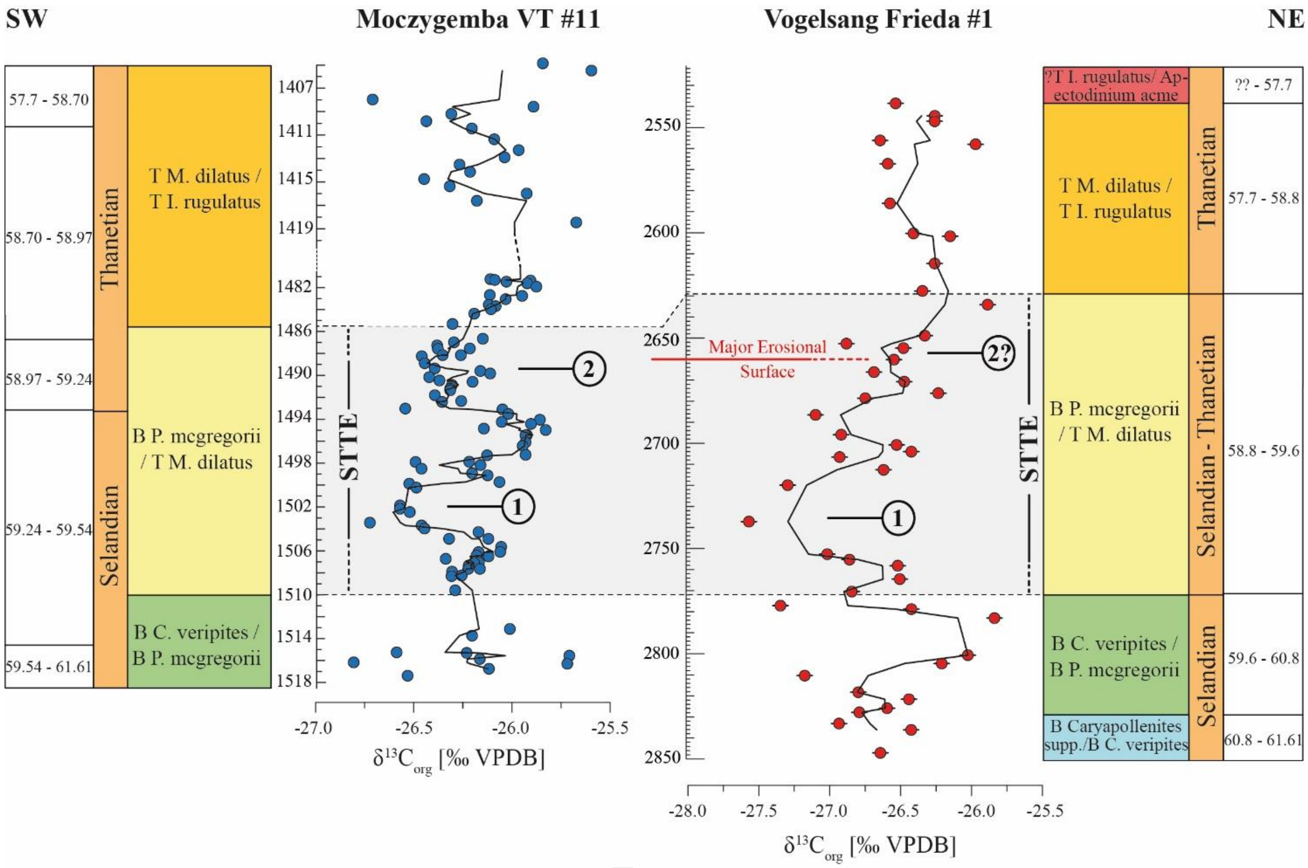

Figure 3. Organic carbon isotope records across the Selandian-Thanetian transition. $\delta^{13}C_{org}$ profiles from the Moczygemba VT #11 (blue circles) and Vogelsang Frieda #1 (red circles) cores plotted against depth, with biostratigraphic and lithostratigraphic frameworks. Key biozones and transitions between the Selandian and Thanetian stages are highlighted, with notable negative carbon isotope excursions (CIEs) indicated with a 5-point moving average. A major erosional surface observed in the Vogelsang Frieda #1 core is also marked (see Figure 1 for more detail).

Weathering and annual precipitation estimates

The Chemical Index of Alteration (CIA) profiles for the Moczygemba VT #11 and Vogelsang Frieda #1 cores reveal distinct weathering patterns across the Selandian–Thanetian interval. In Moczygemba VT #11, CIA values range from 45 to 82%, with an average of 67%, while values in Vogelsang Frieda #1 range from 61 to 79%, averaging 72% (Fig. 4). These values are broadly indicative of moderate to intense chemical weathering and, if accurate, suggest a sustained prevalence of such weathering along the Gulf Coast during this interval. CIA trends across the broader Paleogene succession support this interpretation. During the Paleocene, values remain relatively stable between 69 and 77, approaching but generally staying just below the chemical alteration threshold (CIA = 77). At the Paleocene–Eocene boundary, values increase and cross this threshold, reaching 77 to 83, indicating intensified weathering likely driven by global warming. This peak is followed by a notable decline during the Oligocene, with CIA values falling to 45–65, reflecting diminished weathering intensity under cooler climatic conditions. The CIA values from both cores are consistent with late Paleocene to early Eocene estimates reported by Hessler et al. (2017) and highlight the strong link between chemical weathering intensity and major Paleogene climate transitions.

Mean Annual Precipitation (MAP) estimates from the Gulf Coast cores indicate persistently humid conditions during the late Paleocene to early Eocene, with values ranging from 615 to 1330 mm yr^{-1} (average 1070 mm yr^{-1}) in the Moczygemba VT #11 core and from 960 to 1380 mm yr^{-1} (average 1200 mm yr^{-1}) in the Vogelsang Frieda #1 core (Fig. 4). These estimates are broadly consistent with those from southwestern Wyoming, where paleobotanical data indicate MAP values between 1300 and 1500 mm yr^{-1} during most of the late Paleocene to early Eocene, followed by a decline to approximately 800 mm yr^{-1} under more seasonal and arid conditions later in the interval (Wilf, 2000). High-resolution climate modeling by Sewall and Sloan (2006) similarly reconstructs a humid, tropical to subtropical monsoonal climate across south-central North America during this time, including the southern coastal plain and much of the Laramide foreland. Their simulations suggest that precipitation in these regions was predominantly convective or orographic and sourced from the paleo–Gulf of Mexico. Together, these proxy- and model-based records support the interpretation of warm, wet conditions across much of the continent during the late Paleocene to early Eocene, though with pronounced regional variation controlled by paleogeography, elevation, and atmospheric circulation patterns.

The overall trends in both cores suggest an initial phase of moderate chemical weathering that intensified across the Selandian–Thanetian transition. This shift is mirrored by the highest MAP estimates, indicating a period of enhanced precipitation. Notably, these peaks in weathering and precipitation coincide with negative carbon isotope excursions (CIEs) recorded in both the Moczygemba VT #11 and Vogelsang Frieda #1 cores, linking increased hydroclimatic intensity to short-term carbon cycle perturbations. Following this interval, both CIA and MAP values return to more moderate levels.

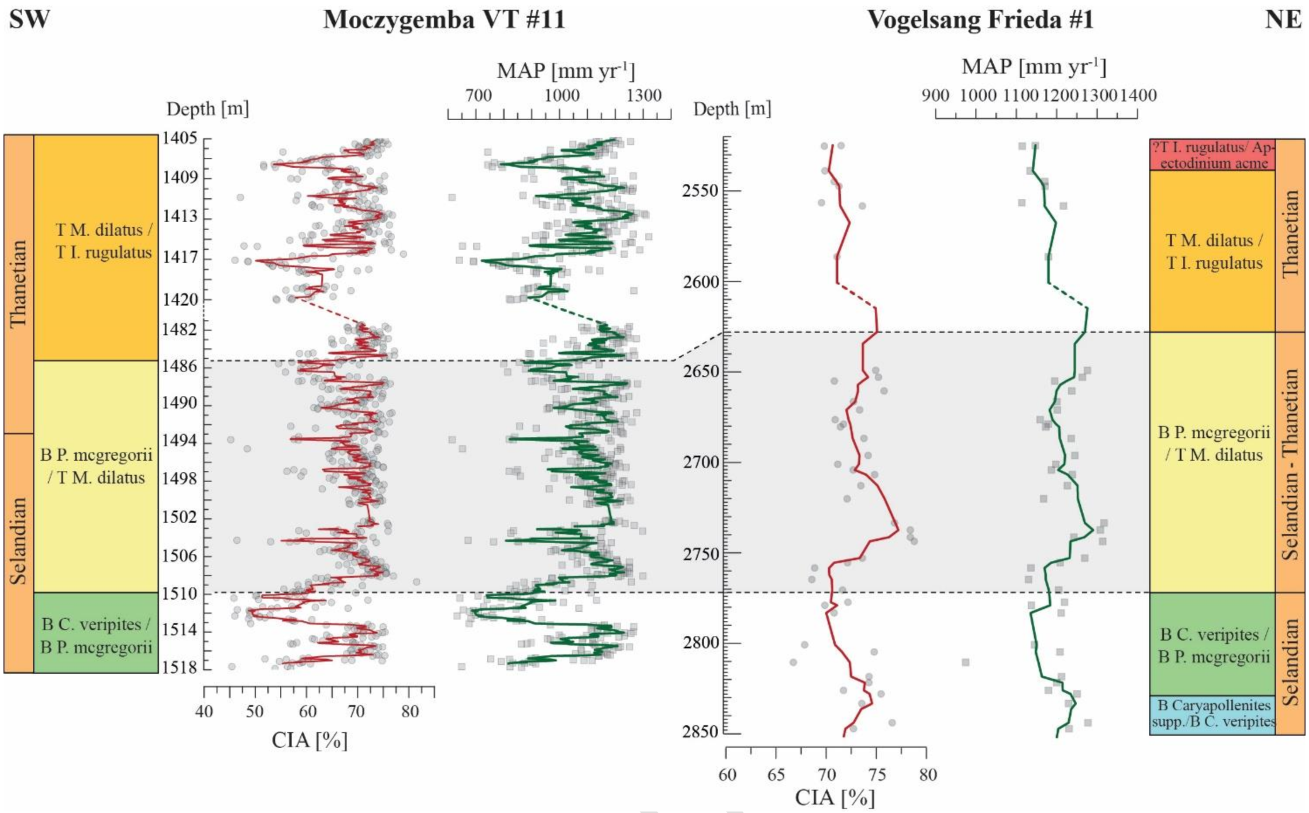

Figure 4. **Chemical weathering and precipitation trends.** Lateral correlation of CIA values and Mean Annual Precipitation (MAP) estimates, represented using a 5-point moving average, for the Moczygemba VT #11 and Vogelsang Frieda #1 cores. The CIA profiles (left panels) indicate variations in chemical weathering intensity, while MAP estimates (right panels) indicate changes in precipitation from the Selandian to the Thanetian. Key biostratigraphic markers are indicated and shaded intervals highlight correlative sections between the two cores.

DISCUSSION

Paleoecology

Palynomorphs

It would normally be expected that palynomorphs produced by more thermophilic organisms would become more common during hyperthermal events, with the caveat that various other factors (differing hydrodynamic properties of palynomorph types, differing susceptibility to degradation by oxidation, etc.) may also influence relative palynomorph abundances. We investigated changes in relative palynomorph abundance by splitting the palynological samples from Moczygemba VT #11 into three groups: a group above the carbon isotope excursion (CIE) near the Selandian-Thanetian boundary (1405-1482 m), a group in the CIE in the Selandian and Thanetian (1482-1505 m), and a group below the CIE in the Selandian (1505-1851 m). Because of the high diversity in palynomorph taxa, the raw specimen counts have been simplified as described in the methods section and analyzed using LDA (Fig. S3, Supplementary Material).

A plot of the first two axes of the LDA for the Moczygemba VT #11 samples is shown in the Supplementary Material files (Fig. S3). The three groups have been outlined with convex hulls and show significant separation. Biplots of the taxa are overlain on the discriminant axis scores for the samples, the length and direction of the vectors indicating the significance of particular taxa in the LDA. The samples in the CIE plot with generally positive discriminant axis scores for both axis 1 and axis 2; only one sample depth in the CIE (at 1486.81 m) falls inside the convex hull of another group. Aside from this outlier, all CIE samples have more positive axis 2 values than the non-CIE samples. A jackknifed confusion matrix (provided in the Supplementary Materials) successfully classified 55% of the samples.

The two taxa with the longest biplot vectors are *Thomsonipollis magnificus* and Betulaceae/Myricaceae type pollen. The biplot vector of *T. magnificus* is nearly vertical upwards, which suggests that higher abundances of *T. magnificus* are associated with the CIE. The Betulaceae/Myricaceae type biplot vector is angled towards the top left quadrant of the graph and suggests that higher abundances of Betulaceae/Myricaceae type pollen are associated with samples above the CIE in the Thanetian. Other taxa with biplots angled towards positive axis 2 values include *Momipites coryloides* (20-27 µm), *Tricolpites hians*, and fungal remains. Taxa with very short biplot vectors, suggesting no significant differences in relative abundance between CIE and non-CIE samples, include *Momipites waltmanensis*, *Classopollis classoides*, and *Deltoidospora microadriennis*.

Although changes in taxa abundance through time are not necessarily related to paleoclimatic change, the LDA results are considered tentative evidence for paleoclimatically induced changes in palynomorph assemblages related to the Selandian/Thanetian hyperthermal. In particular, *T. magnificus* may represent pollen from the Rubiaceae family (Elsik 1968) and has previously been associated with mangrove paleoenvironments (Lenz et al. 2021). Higher abundances of *T. magnificus* may represent an expansion of mangrove paleoenvironments during the CIE. *Momipites coryloides* (20-27 µm) is a form species for pollen morphologically similar to modern *Engelhardia* pollen (Nichols and Ott 1978). Although the extant genus *Engelhardia* is mainly restricted to tropical montane environments, the paleoecological preferences of plants producing *Momipites* pollen in the Paleogene United States appear to be broader, and *Momipites* pollen is abundant in many lowland swamp paleoenvironments in Paleogene strata (Frederiksen 1985). The nearly vertical upwards biplot for *M. coryloides* (20-27 µm) suggests an association with the CIE samples.

The Betulaceae/Myricaceae type is considered to mainly represent pollen from the Betulaceae and Myricaceae families, although identification to modern genera in the Paleogene is problematic (e.g., Jardine 2011). Harrington (2008) observed very high abundances of Betulaceae/Myricaceae type pollen in samples interpreted as representing swamp paleoenvironments in the Paleocene and Eocene of Alabama and suggested that the ecology may be similar to extant coastal strands of *Myrica* shrubs along the Atlantic coast of the United States (Crawford and Young 1998).

Betulaceae/Myricaceae type pollen is associated with post-CIE samples in the LDA graph and may indicate this pollen type is derived from less thermophilic swamp vegetation. *Tricolpites hians* pollen may have an affinity with the Platanaceae (Pocknall and Nichols 1996) but may have been produced by other plant families; in the LDA graph it appears associated more with CIE and post-CIE samples. The biplot vector for fungal remains is angled in the direction of the CIE samples and suggests an association with the CIE.

In order to confirm the significance of the taxa biplots, average relative abundances of selected taxa were calculated for the three sample groups in Moczygemba VT #11 (pre-CIE, CIE, and post-CIE) (see Supplementary Material). In general, these abundances confirm the interpretations from the LDA graph. Average relative abundances of *T. magnificus*, for example, were ca.7.4% in the post-CIE samples, ca.12.7% in the CIE samples, and ca.6.3% in the pre-CIE samples. Relative abundances of *T. magnificus* (relative only to the pollen and plant spore assemblage) have been graphed for both Moczygemba VT #11 and Vogelsang Frieda #1 (Figure S1). *T. magnificus* abundances in Moczygemba VT #11 increase during the Selandian/Thanetian CIE, even exhibiting a double peak at approximately the same depths as the double peak in the carbon isotope data. Although the biplot vector for total dinoflagellate cysts in Moczygemba VT #11 is small and angled towards the upper left quadrant, the raw counts do appear to show two peaks in the CIE section at approximately the same depths as the double peak in *T. magnificus* abundances and carbon isotope ratios (Figure S3), suggesting a potential rise in relative sea level during these hyperthermal events. This relationship is not apparent from the LDA graph (Figure S3), likely because, aside from these two peaks in the CIE section in Moczygemba VT #11, dinoflagellate cyst counts are quite low. An increase in *T. magnificus* abundances is not clearly observed in the CIE of Vogelsang Frieda #1; this may be related to low total pollen abundances in that well introducing more statistical noise, or this could be related to differences in pollen source areas between the two wells.

The relative abundance of fungal remains (calculated relative to the total fungal, pollen, and plant spore assemblage) is higher in the pre-CIE samples than the CIE in Moczygemba VT #11. A notable increase in abundance of fungal spores was observed in a Paleocene-Eocene Thermal Maximum (PETM) section from the southern Gulf of Mexico in the Chicxulub impact crater and interpreted as an indicator for more humid conditions (Smith et al. 2020); in both Moczygemba VT #11 and Vogelsang Frieda #1 there is a general trend towards higher fungal abundances downsection in the Selandian (Figure S3) but there is no clear acme associated with the CIE. There is an overall trend towards decreasing relative abundances of *Classopollis classoides* in the younger Thanetian sections of both Moczygemba VT #11 and Vogelsang Frieda #1, which could be interpreted as a regional contraction of arid coastal paleoenvironments, possibly related to sea level change. However, the decline and eventual extinction of the Cheirolepidiaceae (the plant family which produced *Classopollis* pollen) in the Paleogene globally suggests the decline in *Classopollis* abundance in these wells may be related to competition by angiosperm plants for similar ecological niches rather than a local change in paleoenvironmental conditions (Smith et al., 2024). In summary, the clearest palynological assemblage change during the CIE in Moczygemba VT #11 is an increase in *T. magnificus*, possibly indicating an expansion of mangrove paleoenvironments in response to global warming.

Foraminifera and Nannofossils

The foraminiferal assemblages in Vogelsang Frieda #1 are entirely agglutinated (Figure S1), showing extremely low diversities and strong dominance of *Haplophragmoides* spp., *Ammobaculites* sp., and *Reophax* sp. These taxa are associated with an infaunal life mode, which inhabits below the sediment surface and can tolerate low-oxygen conditions and high nutrient availability (Kaminski and Gradstein, 2005). The shallow marine to deltaic environment in this section suggests that the agglutinated foraminifera were limited for short time periods and adapted to restricted conditions (different from the normal marine shelf), where the main limiting factors were probably the depleted oxygen-concentration and/or nutrient availability in bottom waters throughout the Selandian-Thanetian transition.

Carbon isotopic record

The observed negative $\delta^{13}C_{org}$ excursions may be attributed to several paleoenvironmental and carbon cycle processes. These excursions could be linked to transient warming events, potentially associated with smaller-scale perturbations in the mid to late Paleocene such as the STTE and/or ELPE. The decrease in $\delta^{13}C_{org}$ values suggests an increased contribution of isotopically lighter carbon, which could be derived from enhanced terrestrial organic matter influx due to weathering and soil erosion, methane hydrate destabilization, or shifts in oceanic productivity affecting organic carbon burial (e.g., Arthur et al., 1988; Dickens et al., 1995; Meyers, 1997; Pancost et al., 2007, 2013).

The lateral comparison of $\delta^{13}C_{org}$ profiles from Moczygemba VT #11 and Vogelsang Frieda #1 reveals regionally consistent carbon cycle perturbations across the Selandian–Thanetian transition. The presence of negative excursions, supported by biostratigraphic markers, points to paleoenvironmental changes that warrant further investigation. The observed negative carbon isotope excursions (CIEs) align with coeval records from both marine and terrestrial settings. For instance, a −0.6‰ CIE was identified in the shallow marine Contessa Road section (Gubbio, Italy)

(Coccioni et al., 2019), while significantly larger excursions were reported from terrestrial sections such as Lairière in the northern Pyrenees (−3.7‰; Maufrangeas et al., 2020) and Cerro Bayo in Argentina (−2.9‰ and −4.5‰; Hyland et al., 2015). These terrestrial CIEs are roughly 3–4 times the magnitude of those in shallow marine records, a discrepancy that may reflect differences in carbon reservoir size (Beerling, 2000) and isotopic fractionation between marine and terrestrial organic matter (Sheldon and Tabor, 2009). Alternatively, or additionally, these differences could result from intensified oceanic carbon ventilation and increased petroleum generation in the Gulf of Mexico, analogous to mechanisms proposed for the Early Eocene Climatic Optimum (Hyland et al., 2013).

The $\delta^{13}C_{org}$ values can also serve as indicators of paleoecology and paleoclimate (Kohn, 2010). C_3 plants, which include trees, most shrubs, and cool-season grasses, have $\delta^{13}C$ values ranging from −37‰ to −20‰ and have historically dominated terrestrial vegetation (Kohn, 2010). This broad range of $\delta^{13}C$ values in plants is influenced by factors such as temperature, altitude, latitude, and mean annual precipitation (MAP) (Schulze et al., 1996; Kohn, 2010). Non-water-stressed C_3 plants are enriched in ^{12}C, resulting in more negative $\delta^{13}C$ values, typically below −26‰. In contrast, higher $\delta^{13}C$ values (> −26‰) are associated with plants growing under water-limited conditions and low soil transpiration rates (MAP < 500 mm yr^{-1}) (e.g., Cerling and Quade, 1993; Kohn, 2010). Measured $\delta^{13}C_{org}$ values in both cores suggest the presence of C_3 vegetation during the mid to late Paleocene, confirmed by previous studies such as Cerling and Quade (1993) and Jacobs et al., (1999). While the local climate remains mainly humid during the deposition of Vogelsang Frieda #1, in Moczygemba VT #11, variations in climate can be observed over the depositional period. Humid conditions correspond to negative CIE (lower $\delta^{13}C_{org}$ values) while higher $\delta^{13}C_{org}$ values correspond to a dry ecosystem (MAP ca. 600 mm yr^{-1}).

Apart from paleoecology and paleoclimate interpretations, the presence of isotope excursions allows the lateral correlation of stratigraphic intervals highlighting the use of stable isotopes as a correlation tool in notably difficult to date sub-surface sedimentary successions.

Primary versus diagenetic signals

Changes in composition of the preserved organic matter can influence the observed trends in organic carbon isotope composition and it is as such necessary to evaluate potential diagenetic and secondary overprint on the original geochemical signature before paleoenvironmental interpretations can be carried out.

For this, first, we assessed the relationship between $\delta^{13}C_{org}$ and TOC values (Brasier et al., 1996). Generally, Pearson correlation coefficient (r) less than 0.6 suggest no significant correlation between the isotopic signature and organic matter content (e.g., Fio et al., 2010). In both sections, much lower coefficients were observed ($r < 0.3$) hence there is no significant correlation (Fig. 5). The absence of correlation indicates that the observed negative CIE and the isotopic compositions in general are not due to changes in the TOC content and can therefore be used for paleoenvironmental interpretations (Fig. 5).

Another indicator of diagenesis is the maximum temperature (T_{max}) reached during Rock-Eval pyrolysis (S2), which reflects the thermal maturity of organic matter (OM). In samples with relatively high OM content ($TOC > 0.5$ wt.%; $S2 > 0.2$), the measured T_{max} values were below 440°C (Fig. 5, check Supplementary Material), corresponding to the onset of the oil window (ca.60°C; Espitalié et al., 1985).

These two approaches collectively indicate that the primary isotopic signal is largely preserved in both sections. The data presented can therefore be reliably used to reconstruct paleoclimatic conditions and compare the data with available global isotopic records from the pre-PETM hyperthermal events.

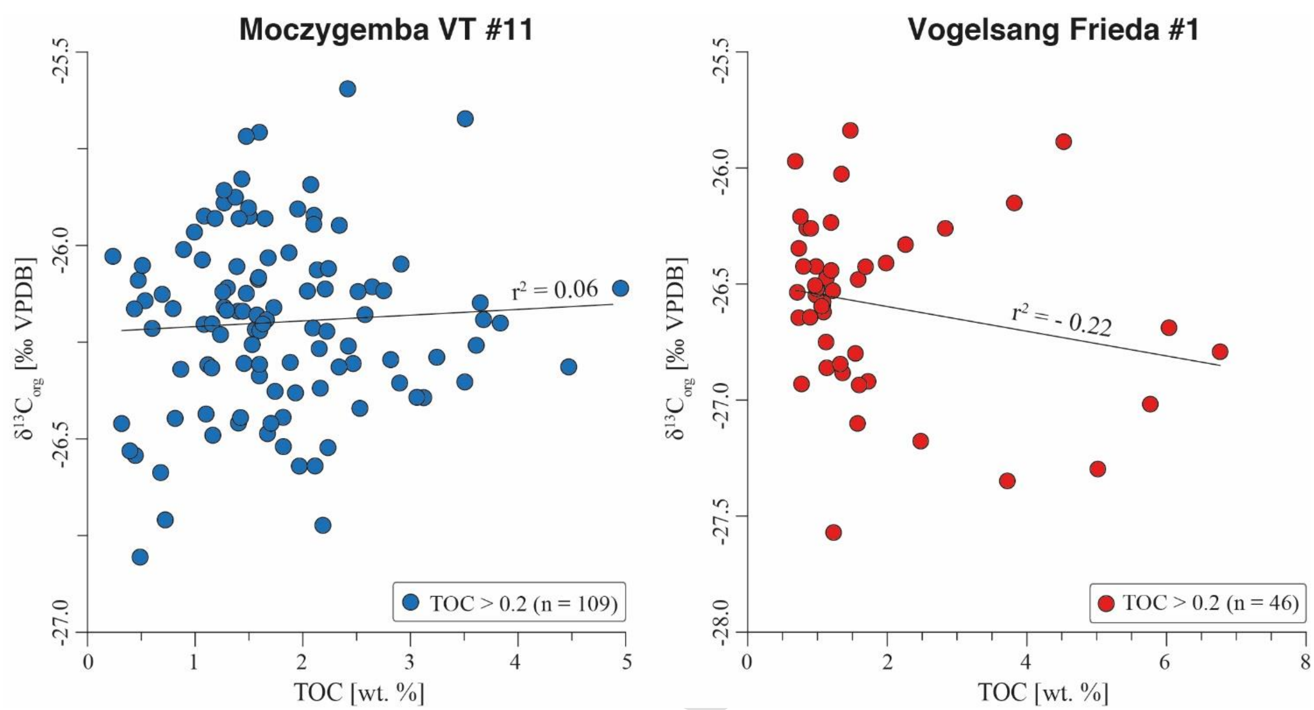

Figure 5. Correlation between TOC and δ[13]Corg in Moczygemba VT #11 and Vogelsang Frieda #1. Scatter plots showing the correlation between total organic carbon (TOC) content (wt.%) and δ^{13}Corg (‰ VPDB) for Moczygemba VT #11 (left, blue circles) and Vogelsang Frieda #1 (right, red circles). The coefficient of determination (r^2) for each dataset is displayed, indicating a non-significant positive correlation in Moczygemba VT #11 ($r^2 = 0.06$) and a non-significant negative correlation in Vogelsang Frieda #1 ($r^2 = -0.22$).

Weathering conditions and regional climate

The observed CIA trends provide valuable insights into the prevailing weathering regimes and regional climate conditions during the Selandian-Thanetian transition. The increasing CIA values in both cores indicate a shift towards more intense chemical weathering, typically associated with warmer and wetter conditions. This trend is consistent with climate reconstructions during global warming periods such as the PETM, which suggest enhanced hydrological cycling in response to global warming and rapid release of carbon (e.g., Chen et al., 2016; Izumi et al., 2018). The slight disparity in CIA and MAP estimates between the two cores may reflect differences in local depositional environments and sediment flux. The consistently higher CIA and MAP values in Vogelsang Frieda #1 suggest a more humid climate regime than Moczygemba VT #11, potentially due to basin topography and proximity to moisture sources. Alternatively, the elevated values in Vogelsang could result from increased detrital sediment input (higher sedimentation rates), creating a more active depositional environment and thus higher CIA and MAP values. The observed differences might also be similar to the Holocene Gulf Coast fluvial systems that span a climate gradient from semi-arid in the southwest to humid in the northeast (Milliken et al., 2017). The CIA values estimated here are slightly lower than those estimated for the PETM, which range between 75 to 85 % (Stokke et al., 2021), but supports the assumption of intense weathering during periods of global warming. The prevailing understanding of Earth's carbon cycle suggests that the negative silicate weathering feedback intensifies in response to rising atmospheric pCO_2 (Colbourn et al., 2015; Penman et al., 2020). Although, the magnitude of this feedback is largely influenced by various local and regional environmental factors, including temperature, precipitation, geomorphology, and lithology (e.g., Richey et al., 2020; Deng et al., 2022). Our observed weathering intensities also align with the predicted semi-arid to humid ecosystem inferred from $\delta^{13}C_{org}$ values, further supporting our interpretation of a locally semi-arid climate and an enhanced hydrological system along the Gulf Coast during the mid to late Paleocene.

The observed regional differences in weathering intensity and precipitation estimates underscore the importance of local paleoenvironmental conditions in modulating broader climatic trends. In conclusion, the combined CIA and MAP reconstructions indicate a trend of increasing weathering intensity and precipitation from the Selandian into the Thanetian, with spatial variations highlighting the interplay between global climate forcing and regional paleoenvironmental factors. These results contribute to a growing body of evidence supporting a warm and humid Middle to late Paleocene climate, with implications for silicate weathering feedbacks and carbon cycle dynamics during this critical interval in Earth's history.

CONCLUSIONS

This study presents the first detailed characterization of the Selandian–Thanetian Transition Event (STTE) within a shallow marine delta system along the Texas Gulf Coast, integrating sedimentological, palynological, and geochemical evidence. Geochemical proxies reveal negative excursions in organic carbon isotopes, intensified chemical weathering, and increased precipitation during the STTE. Palynological data indicate dynamic shifts in coastal vegetation, including the expansion of mangrove-like taxa during inferred hyperthermal phases. While local stratigraphic discontinuities limit signal continuity, comparison with coeval global records supports interpreting this Gulf Coast section as a regional expression of broader Paleocene carbon cycle perturbations. These findings refine the local stratigraphic framework and, more importantly, underscore the sensitivity of marginal marine systems to short-lived hyperthermals, highlighting the value of nearshore archives in complementing both deep-marine and terrestrial isotope records.

ACKNOWLEDGMENTS

We acknowledge financial support from the State of Texas Advanced Resource Recovery Program (STARR) at the Bureau of Economic Geology, Jackson School of Geosciences, Ellington Geological Services, and the Swedish Research Council (grant 2023-04874_VR). Paleontological analyses were specifically supported by Ellington Geological Services. This publication has been approved by the Director of the Bureau of Economic Geology.

REFERENCES CITED

Arthur, M.A., Dean, W.E., Pratt, L.M., 1988. Geochemical and climatic effects of increased marine organic carbon burial at the Cenomanian/Turonian boundary. Nature 335, 714–717. https://doi.org/10.1038/335714a0

Beerling, D.J., 2000. Increased terrestrial carbon storage across the Palaeocene–Eocene boundary. Palaeogeogr., Palaeoclim., Palaeoecol. 161, 395–405. https://doi.org/10.1016/s0031-0182(00)00095-x

Behar, F., Beaumont, V., Penteado, H.L.D.B., 2001. Rock-Eval 6 Technology: Performances and Developments. Oil Gas Sci Technology 56, 111–134. https://doi.org/10.2516/ogst:2001013

Bernaola, G., Baceta, J.I., Orue-Etxebarria, X., Alegret, L., Martín-Rubio, M., Arostegui, J., and Dinarès-Turell, J., 2007, Evidence of an abrupt environmental disruption during the mid-Paleocene biotic event (Zumaia section, western Pyrenees): GSA Bulletin, v. 119, p. 785–795, doi:10.1130/b26132.1.

Blum, M., Pecha, M., 2014. Mid-Cretaceous to Paleocene North American drainage reorganization from detrital zircons. Geology 42, 607–610. https://doi.org/10.1130/g35513.1

Bornemann, A., Jehle, S., Lägel, F., Deprez, A., Petrizzo, M.R., Speijer, R.P., 2021. Planktic foraminiferal response to an early Paleocene transient warming event and biostratigraphic implications. Int. J. Earth Sci. 110, 583–594. https://doi.org/10.1007/s00531-020-01972-z

Bralower, T.J., Silva, I.P., Malone, M.J., and 198, S.P. of L., 2002, New evidence for abrupt climate change in the Cretaceous and Paleogene: An Ocean Drilling Program expedition to Shatsky Rise, northwest Pacific: GSA Today, v. 12, p. 4–10, doi:10.1130/1052-5173(2002)012<0004:nefacc>2.0.co;2.

Brasier, M.D., Shields, G., Kuleshov, V.N., Zhegallo, E.A., 1996. Integrated chemo- and biostratigraphic calibration of early animal evolution: Neoproterozoic–early Cambrian of southwest Mongolia. Geol. Mag. 133, 445–485. https://doi.org/10.1017/s0016756800007603

Cerling, T.E., Quade, J., 1993. Climate Change in Continental Isotopic Records. Geophys Monogr Ser 217–231. https://doi.org/10.1029/gm078p0217

Chen, Z., Ding, Z., Yang, S., Zhang, C., Wang, X., 2016. Increased precipitation and weathering across the Paleocene-Eocene Thermal Maximum in central China. Geochem Geophys Geosystems 17, 2286–2297. https://doi.org/10.1002/2016gc006333

Coccioni, R., Bancalà, G., Catanzarit, R., Fornaciari, E., Frontalini, F., Giusberti, L., Jovane, L., Luciani, V., Savian, J., and Sprovieri, M., 2012, An integrated stratigraphic record of the Palaeocene–lower Eocene at Gubbio (Italy): new insights into the early Palaeogene hyperthermals and carbon isotope excursions: Terra Nova, v. 24, p. 380–386, doi:10.1111/j.1365-3121.2012.01076.x.

Coccioni, R., Frontalini, F., Catanzariti, R., Jovane, L., Rodelli, D., Rodrigues, I.M.M., Savian, J.F., Giorgioni, M., Galbrun, B., 2019. Paleoenvironmental signature of the Selandian-Thanetian Transition Event (STTE) and Early Late Paleocene Event (ELPE) in the Contessa Road section (western Neo-Tethys). Palaeogeogr., Palaeoclim., Palaeoecol. 523, 62–77. https://doi.org/10.1016/j.palaeo.2019.03.023

Colbourn, G., Ridgwell, A., Lenton, T.M., 2015. The time scale of the silicate weathering negative feedback on atmospheric CO2. Global Biogeochem Cy 29, 583–596. https://doi.org/10.1002/2014gb005054

Crabaugh, J. P., & Elsik, W. C., 2000. Calibration of the Texas Wilcox Group to the revised Cenozoic time scale: Recognition of four, third-order clastic wedges (2.7-3.3 my in duration). South Texas Geological Society Bulletin, 41(3), 10–17.

Crawford, E. R., & Young, D. R., 1998. Comparison of gaps and intact shrub thickets on an Atlantic coast barrier island. The American Midland Naturalist, 140(1), 68–77.

Deng, K., Yang, S., Guo, Y., 2022. A global temperature control of silicate weathering intensity. Nat Commun 13, 1781. https://doi.org/10.1038/s41467-022-29415-0

Dickens, G.R., O’Neil, J.R., Rea, D.K., Owen, R.M., 1995. Dissociation of oceanic methane hydrate as a cause of the carbon isotope excursion at the end of the Paleocene. Paleoceanography 10, 965–971. https://doi.org/10.1029/95pa02087

Elsik, W. C., & Crabaugh, J. P., 2001. Palynostratigraphy of the upper Paleocene and lower Eocene Wilcox Group in the northwestern Gulf of Mexico Basin. Proceedings of the IX International Palynological Congress, Houston, Texas, USA, 9, 233–237.

Elsik, W. C., 1968. Palynology of a Paleocene Rockdale lignite, Milam County, Texas, pt. II, morphology and taxonomy (end). Pollen et Spores, 10, 599–664.

Espitalié, J., Deroo, G., and Marquis, F., 1985. Rock-Eval pyrolysis and its applications, Revue De L’Institut Français Du Petrole, 40, 563–579, https://doi.org/10.2516/ogst:1985045

Fio, K., Spangenberg, J.E., Vlahović, I., Sremac, J., Velić, I., Mrinjek, E., 2010. Stable isotope and trace element stratigraphy across the Permian–Triassic transition: A redefinition of the boundary in the Velebit Mountain, Croatia. Chem. Geol. 278, 38–57. https://doi.org/10.1016/j.chemgeo.2010.09.001

Fisher, W.L., & McGowen, J.H., 1967. Depositional systems in the Wilcox Group of Texas and their relationship to occurrence of oil and gas. Austin, TX: Bureau of Economic Geology, University of Texas at Austin, Report of Investigations No. 61, 44 p.

Frederiksen, N., 1985. Review of early Tertiary sporomorph paleoecology. AASP Contributions Series, 15, 1–92.

Galloway, W.E., 2008. Chapter 15 Depositional Evolution of the Gulf of Mexico Sedimentary Basin. Sediment. Basins World 5, 505–549. https://doi.org/10.1016/s1874-5997(08)00015-4

Galloway, W.E., Ganey-Curry, P.E., Li, X., Buffler, R.T., 2000. Cenozoic Depositional History of the Gulf of Mexico Basin. AAPG Bull. 84, 1743–1774. https://doi.org/10.1306/8626c37f-173b-11d7-8645000102c1865d

Galloway, W.E., Whiteaker, T.L., Ganey-Curry, P., 2011. History of Cenozoic North American drainage basin evolution, sediment yield, and accumulation in the Gulf of Mexico basin. Geosphere 7, 938–973. https://doi.org/10.1130/ges00647.1

Gradstein, F. M., Ogg, J. G., Schmitz, M. D., & Ogg, G. M., 2012. The Geologic Time Scale 2012. Elsevier.

Hammer, Ø., Harper, D. A. T., & Ryan, P. D., 2001. PAST: Paleontological Statistics Software Package for education and data analysis. Palaeontologia Electronica, 4(9), 1–9.

Harnois, L., 1988. The CIW index: A new chemical index of weathering. Sediment Geol 55, 319–322. https://doi.org/10.1016/0037-0738(88)90137-6

Harrington, G. J., 2008. Comparisons between Palaeocene–Eocene paratropical swamp and marginal marine pollen floras from Alabama and Mississippi, USA. Palaeontology, 51(3), 611–622.

Hessler, A.M., Zhang, J., Covault, J., Ambrose, W., 2017. Continental weathering coupled to Paleogene climate changes in North America. Geology 45, 911–914. https://doi.org/10.1130/g39245.1

Hewaidy, A.G.A., Farouk, S., Bazeen, Y.S., 2019. The Selandian/Thanetian transition of the Naqb El-Rufuf section, Kharga Oasis, Western Desert, Egypt: Foraminiferal biostratigraphy and sequence stratigraphy implications. J. Afr. Earth Sci. 150, 499–510. https://doi.org/10.1016/j.jafrearsci.2018.10.002

Hyland, E., Sheldon, N.D., and Fan, M., 2013, Terrestrial paleoenvironmental reconstructions indicate transient peak warming during the early Eocene climatic optimum: GSA Bulletin, v. 125, p. 1338–1348, doi:10.1130/b30761.1.

Hyland, E.G., Sheldon, N.D., Cotton, J.M., 2015. Terrestrial evidence for a two-stage mid-Paleocene biotic event. Palaeogeogr., Palaeoclim., Palaeoecol. 417, 371–378. https://doi.org/10.1016/j.palaeo.2014.09.031

Izumi, K., Kemp, D.B., Itamiya, S., Inui, M., 2018. Sedimentary evidence for enhanced hydrological cycling in response to rapid carbon release during the early Toarcian oceanic anoxic event. Earth Planet. Sci. Lett. 481, 162–170. https://doi.org/10.1016/j.epsl.2017.10.030

Jacobs, B.F., Kingston, J.D., Jacobs, L.L., 1999. The Origin of Grass-Dominated Ecosystems. Ann. Mo. Bot. Gard. 86, 590. https://doi.org/10.2307/2666186

Jardine, P., 2011. Spatial and temporal diversity trends in an extra-tropical megathermal vegetation type: The Early Paleogene pollen and spore record from the U.S. Gulf Coast [PhD Dissertation]. University of Birmingham.

Kaminski, M.A., Gradstein, F.M., 2005. Atlas of paleogene cosmopolitan deep-water agglutinated foraminifera. Grzybowski Found. Spec. Publ. 10, 1–574.

Karoui-Yaakoub, N., Mtimet, M.S., Negra, M.H., Grira, C., and Gusemi, W., 2014, The Registration of the Mid-Paleocene Biotic Event (MPBE) in Tunisia: Paleontology Journal, v. 2014, p. 1–5, doi:10.1155/2014/760436.

Kocsis, L., Gheerbrant, E., Mouflih, M., Cappetta, H., Yans, J., and Amaghzaz, M., 2014, Comprehensive stable isotope investigation of marine biogenic apatite from the late Cretaceous–early Eocene phosphate series of Morocco: Palaeogeography, Palaeoclimatology, Palaeoecology, v. 394, p. 74–88, doi:10.1016/j.palaeo.2013.11.002.

Kohn, M.J., 2010. Carbon isotope compositions of terrestrial C3 plants as indicators of (paleo)ecology and (paleo)climate. Proc National Acad Sci 107, 19691–19695. https://doi.org/10.1073/pnas.1004933107

Lenz, O. K., Riegel, W., & Wilde, V., 2021. Greenhouse conditions in lower Eocene coastal wetlands? Lessons from Schöningen, Northern Germany. PLoS ONE, 16(1), e0232861.

Littler, K., Röhl, U., Westerhold, T., and Zachos, J.C., 2014, A high-resolution benthic stable-isotope record for the South Atlantic: Implications for orbital-scale changes in Late Paleocene–Early Eocene climate and carbon cycling: Earth and Planetary Science Letters, v. 401, p. 18–30, doi:10.1016/j.epsl.2014.05.054.

Martini, E., 1971. Standard Tertiary and Quaternary calcareous nannoplankton zonation. Proceedings of the Second Planktonic Conference, Roma 1970., 739–785.

Maufrangeas, A., Leleu, S., Loisy, C., Roperch, P., Jolley, D., Vinciguerra, C., Nguyen-Thuyet, O., 2020. Stratigraphy of the Paleocene continental sedimentary succession of the northern Pyrenean basin (Corbières, southern France) using δ13Corg isotopes. J. Geol. Soc. 177, 752–765. https://doi.org/10.1144/jgs2019-084

McInerney, F.A., Wing, S.L., 2011. The Paleocene-Eocene Thermal Maximum: A Perturbation of Carbon Cycle, Climate, and Biosphere with Implications for the Future. Earth Planet Sci 39, 489–516. https://doi.org/10.1146/annurev-earth-040610-133431

Meyers, P.A., 1997. Organic geochemical proxies of paleoceanographic, paleolimnologic, and paleoclimatic processes. Org. Geochem. 27, 213–250. https://doi.org/10.1016/s0146-6380(97)00049-1

Milliken, K. T., Anderson, J. B., Simms, A. R. and Blum, M. D., 2017, Holocene record of flux of alluvial sediment related to climate: Case studies from the northern Gulf of Mexico, Journal of Sedimentary Research, v. 87, 780–794

Nesbitt, H.W., Young, G.M., 1982. Early Proterozoic climates and plate motions inferred from major element chemistry of lutites. Nature 299, 715–717. https://doi.org/10.1038/299715a0

Nichols, D. J., & Ott, H. L., 1978. Biostratigraphy and evolution of the Momipites-Caryapollenites lineage in the early tertiary in the Wind River Basin, Wyoming. Palynology, 2(1), 93–112.

Pancost, R.D., Freeman, K.H., Herrmann, A.D., Patzkowsky, M.E., Ainsaar, L., Martma, T., 2013. Reconstructing Late Ordovician carbon cycle variations. Geochim. Cosmochim. Acta 105, 433–454. https://doi.org/10.1016/j.gca.2012.11.033

Pancost, R.D., Steart, D.S., Handley, L., Collinson, M.E., Hooker, J.J., Scott, A.C., Grassineau, N.V., Glasspool, I.J., 2007. Increased terrestrial methane cycling at the Palaeocene–Eocene thermal maximum. Nature 449, 332–335. https://doi.org/10.1038/nature06012

Penman, D.E., Rugenstein, J.K.C., Ibarra, D.E., Winnick, M.J., 2020. Silicate weathering as a feedback and forcing in Earth's climate and carbon cycle. Earth-sci Rev 209, 103298. https://doi.org/10.1016/j.earscirev.2020.103298

Petrizzo, M.R., 2005, Proceedings of the Ocean Drilling Program, 198 Scientific Results: Proceedings of the Ocean Drilling Program, doi:10.2973/odp.proc.sr.198.102.2005.

Pocknall, D. T., & Nichols, D. J., 1996. Palynology of coal zones of the Tongue River Member (upper Paleocene) of the Fort Union Formation, Powder River Basin, Montana and Wyoming. AASP Contributions Series, 51, 1–58.

Pujalte, V., Apellaniz, E., Santamaria, F., Monechi, S., Ortiz, S., Orue-Etxebarria, X.,Caballero, F., Rodríguez-Tovar, F., Schmitz, B., 2016. Integrative stratigraphy andclimatic events of a new lower Paleogene reference section from the Betic Cordillera:Río Gor, Granada province. SE Spain. Spanish J. Palaeon. 32, 185–206.

Pujalte, V., Orue-Etxebarria, X., Apellaniz, E., Caballero, F., Monechi, S., Ortiz, S.,Schmitz, B., 2014. A prospective Early Late Paleocene event (ELPE) from the ex-panded Río Gor hemipelagic section (Betic Cordillera, southern Spain): foraminifera,nannofossil and isotopic data. Rend. Online Soc. Geol. It. 31, 181–182.

Richey, J.D., Montañez, I.P., Goddéris, Y., Looy, C.V., Griffis, N.P., DiMichele, W.A., 2020. Influence of temporally varying weatherability on CO2-climate coupling and ecosystem change in the late Paleozoic. Clim Past 16, 1759–1775. https://doi.org/10.5194/cp-16-1759-2020

Rowe, H., Hughes, N., Robinson, K., 2012. The quantification and application of handheld energy-dispersive x-ray fluorescence (ED-XRF) in mudrock chemostratigraphy and geochemistry. Chem. Geol. 324, 122–131. https://doi.org/10.1016/j.chemgeo.2011.12.023

Schulze, E.-D., Ellis, R., Schulze, W., Trimborn, P., Ziegler, H., 1996. Diversity, metabolic types and δ13C carbon isotope ratios in the grass flora of Namibia in relation to growth form, precipitation and habitat conditions. Oecologia 106, 352–369. https://doi.org/10.1007/bf00334563

Sewall, J.O., and Sloan, L.C., 2006, Come a little bit closer: A high-resolution climate study of the early Paleogene Laramide foreland: Geology, v. 34, p. 81–84, doi:10.1130/g22177.1.

Sharma, N., Spangenberg, J.E., Adatte, T., Vennemann, T., Kocsis, L., Vérité, J., Valero, L., Castelltort, S., 2024. Middle Eocene Climatic Optimum (MECO) and its imprint in the continental Escanilla Formation, Spain. Clim. Past 20, 935–949. https://doi.org/10.5194/cp-20-935-2024

Sharman, G.R., Covault, J.A., Stockli, D.F., Wroblewski, A.F.-J., Bush, M.A., 2017. Early Cenozoic drainage reorganization of the United States Western Interior–Gulf of Mexico sediment routing system. Geology 45, 187–190. https://doi.org/10.1130/g38765.1

Sheldon, N.D., Retallack, G.J., Tanaka, S., 2002. Geochemical Climofunctions from North American Soils and Application to Paleosols across the Eocene-Oligocene Boundary in Oregon. J Geology 110, 687–696. https://doi.org/10.1086/342865

Sheldon, N.D., Tabor, N.J., 2009. Quantitative paleoenvironmental and paleoclimatic reconstruction using paleosols. Earth-sci Rev 95, 1–52. https://doi.org/10.1016/j.earscirev.2009.03.004

Sluijs, A., Brinkhuis, H., Schouten, S., Bohaty, S.M., John, C.M., Zachos, J.C., Reichart, G.-J., Damsté, J.S.S., Crouch, E.M., Dickens, G.R., 2007. Environmental precursors to rapid light carbon injection at the Palaeocene/Eocene boundary. Nature 450, 1218–1221. https://doi.org/10.1038/nature06400

Smith, V., Hessler, A., Moscardelli, L., Bord, D., Olariu, I., Lorente, M.A., Sivil, E., Liu, X., 2024. A late refugium for Classopollis in the Paleocene Lower Wilcox Group along the Texas Gulf Coast. Geology. https://doi.org/10.1130/g51772.1

Smith, V., Moscardelli, L., Lorente, M. A., Bord, D., and Olariu, I., 2025. (In press) Quantitative palynology of the Paleocene Lower Wilcox of Texas: Taxonomy, Biostratigraphy, and Paleoecology. BEG Report of Investigation, Austin, Texas.

Smith, V., Warny, S., Grice, K., Schaefer, B., Whalen, M.T., Vellekoop, J., Chenot, E., Gulick, S.P.S., Arenillas, I., Arz, J.A., Bauersachs, T., Bralower, T., Demory, F., Gattacceca, J., Jones, H., Lofi, J., Lowery, C.M., Morgan, J., Otaño, N.B.N., O'Keefe, J.M.K., O'Malley, K., Rodríguez-Tovar, F.J., Schwark, L., Scientists, the I.E. 364, 2020. Life and death in the Chicxulub impact crater: a record of the Paleocene–Eocene Thermal Maximum. Clim. Past 16, 1889–1899. https://doi.org/10.5194/cp-16-1889-2020

Spangenberg, J.E., 2006. Carbon and oxygen isotope working standards from C3 and C4 photosynthates. Isot Environ Healt S 42, 231–238. https://doi.org/10.1080/10256010600841059

Spangenberg, J.E., 2016. Bulk C, H, O, and fatty acid C stable isotope analyses for purity assessment of vegetable oils from the southern and northern hemispheres. Rapid Commun Mass Sp 30, 2447–2461. https://doi.org/10.1002/rcm.7734

Stein, R.A., Sheldon, N.D., Allen, S.E., Smith, M.E., Dzombak, R.M., Jicha, B.R., 2021. Climate and ecology in the Rocky Mountain interior after the early Eocene Climatic Optimum. Clim Past 17, 2515–2536. https://doi.org/10.5194/cp-17-2515-2021

Stokke, E.W., Jones, M.T., Riber, L., Haflidason, H., Midtkandal, I., Schultz, B.P., Svensen, H.H., 2021. Rapid and sustained environmental responses to global warming: the Paleocene–Eocene Thermal Maximum in the eastern North Sea. Clim Past 17, 1989–2013. https://doi.org/10.5194/cp-17-1989-2021

Styzen, M. J., 1997. Cascading counts of nannofossil abundance. Journal of Nannoplankton Research, 19(1), 49.

Sweet, M. L., & Blum, M. D., 2012. Paleocene-Eocene Wilcox Submarine Canyons and Thick Deepwater Sands of the Gulf of Mexico: Very Large Systems in a Greenhouse World, Not a Messinian-Like Crisis. Search and Discovery Article #90158.

Traverse, A., 2007. Paleopalynology (2nd ed., Vol. 28). Springer.

Vimpere, L., Spangenberg, J.E., Roige, M., Adatte, T., Kaenel, E.D., Fildani, A., Clark, J., Sahoo, S., Bowman, A., Sternai, P., Castelltort, S., 2023. Carbon isotope and biostratigraphic evidence for an expanded Paleocene–Eocene Thermal Maximum sedimentary record in the deep Gulf of Mexico. Geology 51, 334–339. https://doi.org/10.1130/g50641.1

Westerhold, T., Röhl, U., Donner, B., McCarren, H.K., and Zachos, J.C., 2011, A complete high-resolution Paleocene benthic stable isotope record for the central Pacific (ODP Site 1209): Paleoceanography, v. 26, doi:10.1029/2010pa002092.

Westerhold, T., Röhl, U., Donner, B., McCarren, H.K., Zachos, J.C., 2011. A complete high-resolution Paleocene benthic stable isotope record for the central Pacific (ODP Site 1209). Paleoceanography 26. https://doi.org/10.1029/2010pa002092

Wilf, P., 2000, Late Paleocene–early Eocene climate changes in southwestern Wyoming: Paleobotanical analysis: GSA Bulletin, v. 112, p. 292–307, doi:10.1130/0016-7606(2000)112<292:lpecci>2.0.co;2.

Zachos, J.C., Dickens, G.R., Zeebe, R.E., 2008. An early Cenozoic perspective on greenhouse warming and carbon-cycle dynamics. Nature 451, 279–283. https://doi.org/10.1038/nature06588

Zachos, JC., Kroon, D., Blum, P., Bowles, J., Gaillot, P., Hasegawa, T., Hathorne, EC., Hodell, DA., Kelly, DC., Jung, J.-H., Keller, SM., Lee, YS., Leuschner, DC., Liu, Z., Lohmann, KC., Lourens, L., Monechi, S., Nicolo, M., Raffi, I., Vallius, H., 2004. Early Cenozoic extreme Climates: The Walvis Ridge transect, Proceedings of the Ocean Drilling Program, Initial reports Leg 208. Proceedings of the Ocean Drilling Program: Initial Reports. http://www.ldeo.columbia.edu/BRG/ODP/ODP/LEG_SUMM/208/leg208.html

Zarra, L., Hackworth, R., & Kahn, A., 2019. Wilcox Chronostratigraphic Framework Update. AAPG Search and Discovery Article, 51616. https://doi.org/10.1306/51616Zarra2019

Zeng, H., and Olariu, I., 2024. Machine-learning-assisted seismic prediction of massive (up to 500m) sands and their geologic meaning: Lower Wilcox intraslope basins, south-central Texas, USA: Marine and Petroleum Geology, v. 167, 106935

Zhang, J., Ambrose, W., Steel, R., Chen, S., 2022. Long cores through the Wilcox Group, Gulf of Mexico, show process variability across different time scales. AAPG Bull. 106, 1404–1429. https://doi.org/10.1306/02072220097

Zhang, J., Covault, J., Pyrcz, M., Sharman, G., Carvajal, C., Milliken, K., 2018. Quantifying sediment supply to continental margins: Application to the Paleogene Wilcox Group, Gulf of Mexico. AAPG Bull. 102, 1685–1702. https://doi.org/10.1306/01081817308

[1]Supplemental Material. *[Please provide a brief description of your material.]* Please visit https://doi.org/10.1130/XXXX to access the supplemental material, and contact editing@geosociety.org with any questions.